STScI | SPACE TELESCOPE SCIENCE INSTITUTE

Instrument Science Report ACS 2018-03

A Minor Contamination Event in May 2017 Affecting the ACS/WFC CCDs

S.L. Hoffmann, N. Miles, J.E. Ryon, N. Hathi & N.A. Grogin

May 25, 2018

Abstract

Here we present our investigation of three image artifacts that recently appeared in images from Hubble's Advanced Camera for Surveys (ACS) Wide Field Channel (WFC). We discovered one of the artifacts through visual inspection of a WFC image during an unrelated task. A search of routine calibration data revealed that it, and two additional artifacts, appeared on May 5th, 2017. We named the three image artifacts "flecks" because they looked to be small flecks of material sitting on the surface of the WFC detector in our initial examination. We characterized the flecks by analyzing them in routine calibration images. Due to their small size, we do not believe the flecks will have an impact on science use of ACS/WFC. Finally, while we believe the appearance of the flecks to be an isolated incident, we will continue to monitor ACS/WFC images for new flecks in the future.

1 Introduction

In order to enable the astronomical community to achieve the most accurate scientific results, the ACS team applies a host of calibrations to improve image quality. This is due to the simple fact that no detector is perfect, and that continued exposure of any instrument to the radiation environment of space leads to inevitable degradation. Before ACS was installed on *HST*, a number of inconsequential defects, called "freckles", were found on the WFC

detectors. As described in Bohlin et al. (2001), freckles are typically the size of a few pixels and have been stable over the life of the instrument. Few have a flux loss of more than 50%, and the flat field calibration successfully corrects the freckles in the science images. No new freckles or other such image artifacts have been discovered until recently.

In this report, we discuss three newly appearing image artifacts named "flecks". We describe the discovery (§ 2) and initial examination (§ 3) of the flecks. We detail our analysis of the flecks in various calibration and reference images (§ 4-6) to determine their characteristics. Finally, we discuss automated detection and monitoring going forward (§ 7) as well as the conclusions of our analysis (§ 8).

2 Discovery

The larger fleck was discovered in November 2017 during verification of updates to the cosmic ray rejection algorithm in `ACSREJ`, which is a module of the `ACSTOOLS` software[1]. As part of the verification process, a random sample of anneal cycles spanning the lifetime of ACS were processed with `ACSREJ` and analyzed. We first identified the presence of the larger fleck during analysis of the anneal cycle covering June 26th to July 26th, 2017, as shown in Figure 1.

Discovery of the flecks occurred several months after their appearance due to the process established by the ACS Team to generate post-flashed calibration darks (Ogaz et al., 2015). Since January 2015, all calibration darks have been post-flashed to ameliorate the charge transfer efficiency (CTE) losses of the WFC charge-coupled devices (CCDs). This required a fundamental change in the way superdarks are created from data taken for the CCD Daily Monitor calibration program 14946 (PI: Desjardins). Approximately every two days, the Daily Monitor program observes four 1000.5 s darks, post-flashed for 4.6 s, and two 0.5 s darks, also post-flashed for 4.6 s. At the end of the anneal cycle, all of the long exposure darks are combined to make a single, high signal-to-noise (S/N) base dark, while all of the short exposure darks are combined to create a single, high S/N short dark. Next, the set of four long darks observed on a given day are combined to create a daily dark. This daily dark is used to propagate information about transient hot pixels into the base dark for that day. The combination of a daily dark and the base dark is colloquially referred to as a daily superdark. The last step in making non-CTE corrected darks is to subtract the short dark from the daily superdarks to remove the post-flash signal. To produce the CTE-corrected daily superdark, the pixel-based CTE correction, as described in Anderson & Bedin (2010), is applied to both the short dark and the daily superdarks, and then the short dark is subtracted from each of the daily superdarks. Finally, after visual and statistical inspection, the daily superdarks are delivered to the Calibration Reference Data System (CRDS) for use in the `DARKCORR` step of `CALACS`.

By differencing pairs of darks with identical post-flash durations, the larger fleck is effectively removed from the daily superdark, as shown in Figure 2. Because visual and statistical analysis is only performed on the daily superdark, the flecks evaded discovery for a short time. After the larger fleck was found, a visual analysis of recent single short darks established that the fleck appeared after the last observation of the April 4th to May 3rd anneal

[1] http://acstools.readthedocs.io/en/latest/index.html

cycle, but before the first observation of the next anneal cycle from May 5th to May 29th. The first image of the fleck was taken on May 5th, which we define to be the date of origin. With the date of origin established, a search for other new flecks was conducted, and resulted in the identification of two additional flecks appearing on the same day. We show all three flecks in Figure 3.

3 Initial Characterization

Next, we determined whether the flecks are a malfunction in the CCD (e.g. groups of sink pixels) or particulate material located in the optical path between the LED and the CCD. To this end, we examined un-flashed darks covering the same time period. If the flecks are caused by a malfunction in the CCD, then the profile of the fleck-affected pixels should be identical in un-flashed and flashed darks. If the flecks disappear in un-flashed data, then we know that they are caused by a particulate in the optical path between the CCD and the LED.

As part of the ACS CCD Hot Pixel Annealing calibration program 14951 (PI: Desjardins), four un-flashed 1040 s dark frames are taken within the 12 hours before annealing the detector, and another four un-flashed 1040 s dark frames are taken within 12 hours after completing the annealing process. We bias-corrected and combined each set of four with `ACSREJ` to reject cosmic rays and increase the S/N ratio. In Figure 4, we show that the fleck disappears in the un-flashed data, along with the expected trailing behavior of hot pixels in 1000 s of dark current accumulation. This implies that the flecks are the shadows of new particulate material in the optical path. Because the shadows of the flecks are fairly well defined, they are most likely located on the surface of the CCD. This suggests that they originated from within the CCD housing. Finally, a rough count of the pixels comprising the fleck based on visual inspection finds that the area of the larger fleck is approximately 144 pixels and the elongated fleck is 52 pixels. Given that the ACS/WFC pixels are 15 μm $\times$ 15 μm in size, an upper limit on the sizes of the larger fleck and the elongated fleck at the widest point are 0.0324 mm^2 and 0.0117 mm^2, respectively.

4 Comparison of the Flecks in Two Epochs of EPER Flats

To further characterize the flecks, two epochs of extended pixel edge response (EPER) lamp images are available. EPER images are obtained on a regular cadence to monitor relative CTE losses from the ACS/WFC detectors over time. Average signal levels between 180 and 42,000 e^- are reached by observing the internal Tungsten lamp for a range of exposure times and filter pairings. Most recently, EPER images were obtained on May 10th, 2017 for CAL/ACS program 14508 (PI: Chiaberge) and again on November 13th, 2017 for CAL/ACS program 14950 (PI: Ryon). We can inspect these data for any changes in the position and shape of the flecks over the 6-month period between observations.

We first remove a constant bias level, measured from the physical prescan, from each raw EPER image. We then pair the EPER images from the two epochs by signal level and

take the ratio of the November 2017 image to the May 2017 image. Figures 5 through 7 show the results for the larger fleck, the elongated fleck, and the tiny fleck, respectively. Each figure contains six panels, one for each EPER flat signal level, and each panel shows a 40×40 pixel region from the November 2017 to May 2017 ratio image containing the fleck in question. The background becomes noticeably less noisy as signal level increases. For each ratio image, the mean of a small rectangular region containing each fleck lies between 0.97 and 1.04, suggesting there is little change in the transmissivity of each of the flecks with time. The standard deviation of pixel values within the flecks themselves is often higher than nearby empty regions, but this is expected for a dark, low-level feature.

In Figure 5, residuals from the ratio image are visible at the location of the larger fleck in each panel, but no clear structure is seen. The elongated fleck, however, does appear to have some minor structure in the middle and right bottom panels of Figure 6, with a brighter bottom half and darker top half. The peak of the bright region is about 5% brighter than the local average, and the peak of the dim region is about 10% below average. This structure suggests the fleck may have shifted slightly in the negative y-direction between May 2017 and November 2017. Absolutely no structure is seen in Figure 7, likely because this fleck is very small with higher transmissivity than the others.

5 Low-level Trails from the Larger Fleck

In flashed short darks, the larger fleck appears to display a "shadow" in the positive y-direction. This can be seen in Figure 8. To test whether the signal level in the shadow is significantly lower than the local background, we calculate the total signal in the 11×3 pixel region outlined in blue in Figure 8, and also in an empty region of the same size to the right ($+x$) of the fleck. The noise in the measurement is simply the square root of the total signal, from Poisson statistics. We perform the same calculations on each average short dark obtained between January 2015 and January 2018, and plot the result in Figure 9. For all of the short darks taken before May 2017, the signal in the shadow region and the empty background region agree within the noise. Once the fleck appears, the total shadow signal drops significantly below the typical background level, by almost 200 e^-.

The shadow is therefore a real feature in the short dark images and may have an origin similar to that of sink pixel trails. Sink pixels are locations of extreme charge trapping in the WFC detectors (Ryon & Grogin, 2017). Many sink pixels give rise to low-valued trails in the direction away from the serial register ($+y$ in WFC2), in the same direction as the shadow appears relative to the fleck. Sink pixel trails are likely due to further trapping of electrons in pixels that travel through the sink pixel during readout. Therefore, if the local background is low, there will be more traps available in a given sink pixel and the trail will be longer than if the local background were high. A similar phenomenon may be taking place with the pixels in the larger fleck. Though they may not be true sink pixels, the pixels within the fleck are subject to a much lower background than the rest of the image, and therefore may be trapping extra electrons during readout, giving rise to the shadow.

6 Photometric Analysis

6.1 Lamp Flats

Flat fields are acquired every six months as part of the routine calibration of ACS/WFC. On 1 December 2017, soon after the discovery of the flecks, the CAL/ACS 14954 program obtained flat field images with the Tungsten lamp in 12 filters (Avila et al., 2017). The filters are listed in Table 1, along with the exposure time and the median value in electrons (e^-) of the entire CRC image to demonstrate the amount of flux found in these images. The CRC image is a combination of three exposures that were cosmic ray-rejected, CTE-corrected, and delivered by the MAST archive. An inspection of the newly acquired flat field data revealed the presence of all three flecks. Figures 10 & 11 show the larger fleck and the elongated fleck, respectively, in flat images for 8 broadband filters from 2016 and 2017. The tiny fleck at (1850, 1755) on WFC1 is not included in the photometric analysis due to its small size and close proximity to another artifact.

We defined an aperture for photometric analysis of the larger fleck as follows. We selected a 40×40 pixel subsection of the image that centered the larger fleck at position (1521, 1773) on the WFC2 chip. We divided out the local median to remove the background and then derived the inverse of the image by subtracting all the pixels from unity. This centers the main distribution of background pixels at zero and changes the fleck measurements to appear similar to radiating sources. We show the inverted subsection of the F435W flat image in Panel A of Figure 12, along with a histogram that shows the percentage of expected flux not transmitted in Panel B. A natural break occurs at 5%, marked by a vertical orange line. We used this threshold to define the photometric aperture for F435W. All the pixels that block more than 5% of the flux as compared to the local background are associated with the fleck, and therefore are used to define the aperture. We plot a mask of the aperture to show the shape in Panel C.

We repeated this analysis for the other 7 filters and produced a total of 8 individual apertures. We then summed the masks to create the master photometric aperture, so that the master aperture contains every selected pixel from the individual apertures. In Figure 13, the shape of the master photometric aperture is outlined in red. The grayscale demonstrates the frequency with which each of the aperture pixel is selected. Black means the pixel is not part the aperture in any of the filters, white means the pixel was selected in all of them, and the gray tones map the range in between. We applied the master aperture to the normalized subsection of the flat in each filter, an example of which we show in Figure 13 for F435W, and summed the pixels.

The normalization of the flat subimages means that each pixel should equal unity. Summing the pixels inside the aperture and then dividing by the size of the aperture should likewise produce unity. However, we measure lower values due to the obstruction of the fleck. We show the percentage below the expected 100% transmissivity in Figure 14 which can be interpreted similar to a spectral energy distribution (SED) where the transmissivity is plotted against the effective wavelength of the Tungsten lamp spectrum (Johnson, 1997, 1998) convolved with the filter passbands. Each point represents an average measurement over the size of the master aperture, with the pixels at the edges contributing much of the measurement and the transmissivity dropping to zero at the center of the fleck. The SED

Table 1. CAL/ACS 14954 observations

Filter	Exp. Time (seconds)	Image Median (e^-)	Filter	Exp. Time (seconds)	Image Median (e^-)
F435W	52.8	180653	F625W	9.0	167525
F475W	16.2	176405	F658N*	150.0	–
F502N*	372.0	–	F660N*	420.0	–
F550M*	20.4	–	F775W	11.1	142623
F555W	12.0	169050	F814W	8.7	177182
F606W	6.9	205767	F850LP	12.6	163937

*Narrowband filters were not included in the photometric analysis.

Note. — The median values are measured from a single image produced by combining three cosmic ray-rejected and CTE-corrected exposures.

stays nearly constant across the wavelength range with the exception of an abrupt rise at redder wavelengths in filters F814W and F850LP.

We performed the same analysis on the elongated fleck at (3510, 355) on WFC1, though we used a 20×30 pixel subsection to better match the size of the fleck. Figure 15 shows the inverted, normalized flat image, the master aperture, and that aperture applied to the F435W image. Finally, the SED in Figure 16 shows similar behavior to that of the larger fleck in Figure 14 with the exception of the dip in the F555W band. We find about twice as much error in the error array of the F555W image as compared to the other filters when we average the values of the error array inside the master aperture. Therefore, while the exact cause of this discrepancy is not known, we believe it to be anomalous and not a real feature of the fleck material.

However, we do believe the upturn at red wavelengths is a real phenomenon. We investigated the possibility of contamination due to the red halo, where red photons pass completely through the silicon wafer of the CCDs, scatter diffusely off the soda-glass substrate and travel back into the silicon to be detected as a halo of increased flux around sources. The WFC CCD, however, has a layer of gold between the silicon and the soda-glass which reflects red photons instead of scattering them and returns them to the pixel through which they originally passed, nearly eliminating any potential red halo below 9000 Å. We see this empirically in the encircled energy for 1.0″ in Figure 1 of Bohlin (2011). We examine the L3.5V star $2M0036+18$ as the closest match to the behavior of the Tungsten flat lamp at red wavelengths and find an approximate 2.5% drop in the flux between F775W and F850LP, presumably due to the red halo. This is well below the changes we measure in the fleck photometry between F775W and F850LP of 7.6% and 7.1% for the larger and elongated flecks, respectively, and therefore we rule out red halo as the cause.

6.2 LED Post-Flash

We repeated the photometric analysis on the post-flash reference file that is created from pairs of dark frames that are post-flashed (see Miles (2018) for additional details). The post-flash illuminates with an LED instead of the Tungsten lamp, so the difference between the

spectra could provide another data point for the SED. We applied the master photometric aperture created for the flats to the post-flash reference, as shown in Figure 17. The aperture does not fit the shape and location of the fleck in the post-flashed darks as well as it does the flat data as seen in Figures 13 and 15. We found the position and shape of the flat aperture to be stable for all bandpasses, so this discrepancy is not a result of wavelength dependence. Instead, it is an inherent difference in the apparent shape of the fleck when illuminated with the LED.

We then generated an aperture for the post-flash reference file using the same technique as for the flat aperture. The difference of the two apertures is shown in Figure 17. The discrepancy between the apertures is of the same magnitude and in the same direction for both the larger and elongated flecks. Since the two flecks are on separate chips, this points to a fundamental difference between the flats and the post-flashed darks that cannot be explained by any localized features. We determined that the change is due to the shifted light path between the LED and the Tungsten lamp. The angle at which the light hits the fleck material due to these different light paths causes the difference in shape and size of the flecks between the flat field and post-flash reference images. Additionally, we see a slight enhancement in flux above the fleck in the flat images (see Figures 10 and 11), possibly due to reflection off the material of the fleck. The flux in this reflection is small enough to fall within the poisson distribution associated with the background, but the fact that it is not visible in the reference images illuminated with the LED (see Figure 3) is another indicator of a light path difference.

The discrepancy in the shape and size of the fleck introduces too many variables to make an accurate measurement of the transmissivity with the same technique used for the flats. Therefore, we go no further with the photometric analysis of the post-flashed darks other than to note that we measure a similar large drop in flux at the fleck positions.

7 Detection and Future Monitoring

In order to locate and monitor the flecks and other fleck-like artifacts, such as the freckles from Bohlin et al. (2001), we develop an automated fleck-searching method. Our method is very similar to the WFC3 blob-searching technique (McCullough et al., 2014) with a couple of key differences. First, we used flashed dark exposures from the CCD Daily Monitor program (PI: Desjardins), which are obtained frequently, instead of flats, which we observe approximately every 6 months with program 14954 (PI: Hoffmann). Second, ACS flecks are not symmetrically round and star-like, unlike the WFC3 blobs (Pirzkal et al., 2010), so we use a different algorithm compared to WFC3 to search for these flecks.

After exploring various types of flashed darks, we chose to use short (0.5 sec) flashed dark images because they have the strongest contrast between fleck pixels and the background, which is very important to identify flecks with an automated approach. We used short flashed darks obtained between April 2017 and September 2017 to identify and confirm the three manually-discovered flecks that appeared in ACS/WFC images around May 5th, 2017.

To identify image artifacts, we began with one of the combined and averaged CTE-corrected short flashed dark image (the DKC file) created for each anneal cycle. We median-filtered the image with a 15×15 pixel kernel to remove individual deviant pixels. We then

subtracted the pixel values from unity to make the flecks appear as positive deviations and multiply by 100, causing any artifacts to appear like stars or galaxies above a background of zero. These image manipulation steps are very similar to WFC3 blob-searching technique as outlined in McCullough et al. (2014).

We used source extraction software, SExtractor (Bertin & Arnouts, 1996), instead of the star-finding algorithm used by WFC3 to identify flecks because the flecks are not symmetrical. We found ~ 100 artifacts with `DETECT_THRESH` set to 5.0 sigmas above the background noise and `DETECT_MINAREA` to 25 pixels. The majority of these detections are small (< 6 pixels wide) and do not block more than 50% of the flux, and as such we expect the flat field calibration to properly correct for these artifacts. Also, we want to stress that with the exception of the three flecks in May 2017, no new image artifacts appear at any time in the ACS/WFC lifetime. We verified through visual inspection of the flats that all the detections (except the 3 new flecks) are freckles that exist and are stable throughout the lifetime of the instrument. Figure 18 shows example images of both the flecks and the other artifacts found with our automated procedure.

We will continue to monitor ACS/WFC images to ensure the flecks do not change with time, as well as identify any new image artifacts that might appear in the future.

8 Conclusion

The fact that we determined the flecks to be particles on the surface of the WFC CCDs limits the potential sources to material inside the CCD housing. The three most likely culprits behind the flecks are as follows. 1) Delamination of the black anti-reflection coating applied to prevent light scattering off the CCD housing. 2) Metal flakes dislodged from loosened screws inside the inner cavity. It was hypothesized that the repeated temperature variations due to the anneal cycles could have loosened the screws. However, even if this is the case, ACS/WFC has undergone monthly anneals over its entire lifetime, and it would therefore be illogical to stop the anneals simply because of one adverse occurrence in a single anneal cycle. 3) Indium shed from the window-to-shield joint caused by vibration.

Our analysis cannot conclusively distinguish between these sources, but in all three cases, the same actions would be required. We marked the pixels associated with the flecks which have less than 50% transmissivity (a total of 67 pixels for the larger fleck and 21 for the elongated fleck, see the histograms in Figures 12 and 15, respectively) as bad pixels using the bad pixel flag value of 4 in the bad pixel table (bpixtab) reference file as of May 5th, 2017. This information propagates to the data quality (DQ) image and allows the pixels affected by flecks to be identified and appropriately processed during image drizzling. For science cases which cannot tolerate any holes in the image caused by the flecks, we recommend using the default ACS-WFC-DITHER-LINE dither pattern. It was created to remove the chip gap and will be more than enough of an offset to provide coverage of the small flecks. The ACS Team recommends that WFC observers consult their assigned Program Coordinator if concerned about potential science impact from these flecks.

Finally, we have not found any flecks in the ~ 12 months since these three appeared. We emphasize that this was an isolated event and that the ACS team will monitor the WFC detector in the future for new image artifacts.

Acknowledgements

This research made use of Astropy, a community-developed core Python package for Astronomy (Astropy Collaboration et al., 2013), and the Matplotlib Python plotting library (Hunter, 2007).

The authors would like to thank ACS team members Ralph Bohlin and Marco Chiaberge for their useful comments. We also thank our colleagues David Golimowski and George Hartig for helpful conversations during this work.

References

Anderson, J., & Bedin, L. R. 2010, PASP, 122, 1035

Astropy Collaboration, Robitaille, T. P., Tollerud, E. J., et al. 2013, A&A, 558, A33

Avila, R., et al. 2017, Advanced Camera for Surveys Instrument Handbook for Cycle 25 v. 16.0 (STScI)

Bertin, E., & Arnouts, S. 1996, A&AS, 117, 393

Bohlin, R. C. 2011, Flux Calibration of the ACS CCD Cameras II. Encircled Energy Correction, Tech. rep., STScI

Bohlin, R. C., Hartig, G., & Martel, A. 2001, HRC and WFC Flat Fields: Standard Filters, Polarizers, and Coronograph, Tech. rep., STScI

Hunter, J. D. 2007, Computing In Science & Engineering, 9, 90

Johnson, E. H. 1997, Characterization of EXP-0369 Tungsten Lamp, Tech. rep., Ball Aerospace & Technologies

—. 1998, ACS Throughput Model, Tech. rep., Ball Aerospace & Technologies

McCullough, P. R., Mack, J., Dulude, M., & Hilbert, B. 2014, Infrared Blobs : Time-dependent Flags, Tech. rep., STScI

Miles, N. 2018, Updates to Post-Flash Calibration for the Advanced Camera for Surveys Wide Field Channel, Tech. rep., STScI

Ogaz, S., Anderson, J., & Golimowski, D. 2015, Post-Flash Calibration Darks for the Advanced Camera for Surveys Wide Field Channel (ACS/WFC), Tech. rep., STScI

Pirzkal, N., Viana, A., & Rajan, A. 2010, The WFC3 IR "Blobs", Tech. rep., STScI

Ryon, J. E., & Grogin, N. 2017, Sink Pixels in ACS/WFC, ACS ISR 2017-01, STScI

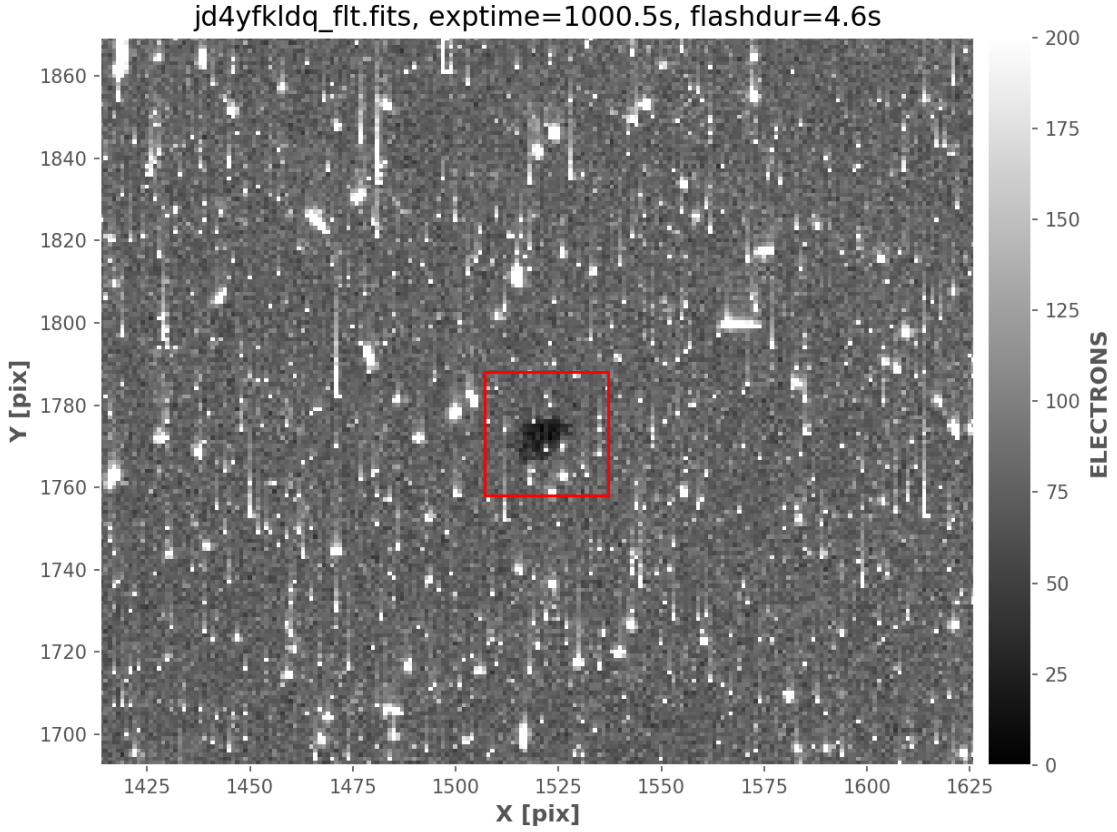

Figure 1 - A region in the flashed long dark image from the June 26th to July 26th 2017 anneal cycle with the larger fleck highlighted by the 20×20 pixel red square.

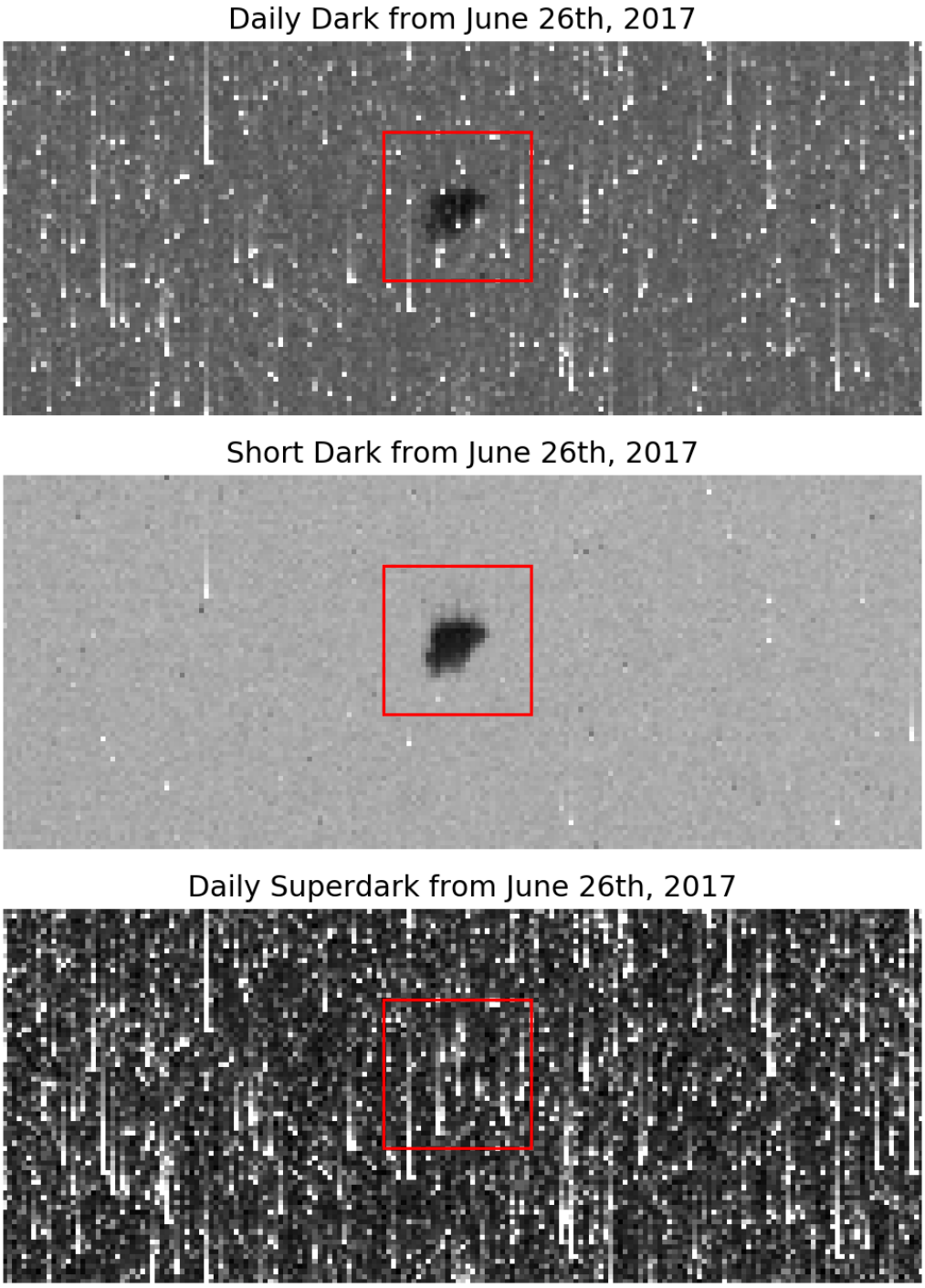

Figure 2 - The effect of differencing the daily dark and the short dark for the June 26th to July 26th 2017 anneal cycle. The top image is a daily dark, the middle image is the short dark, and the bottom image is the daily superdark. The 20×20 pixel red square is centered on the location of the fleck in each of the three images. While the fleck is readily apparent in the daily dark and the short dark, it is non-existent in the daily superdark.

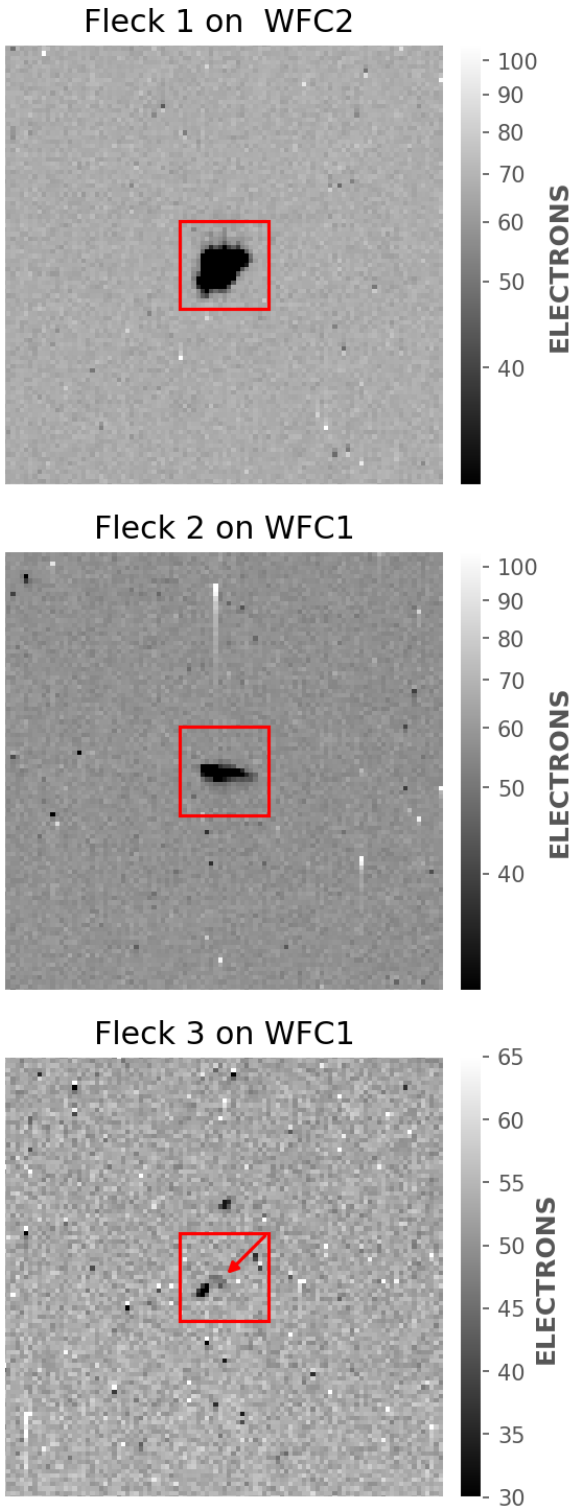

Figure 3 - The three flecks identified by the ACS Team. A 20×20 pixel red square is shown for scale. The larger fleck (top panel, 1) is on WFC2 at (1521, 1773). The other flecks are on WFC1: the elongated fleck (middle panel, 2) at (3510, 355) and the tiny fleck (bottom panel, 3) at (1850, 1755).

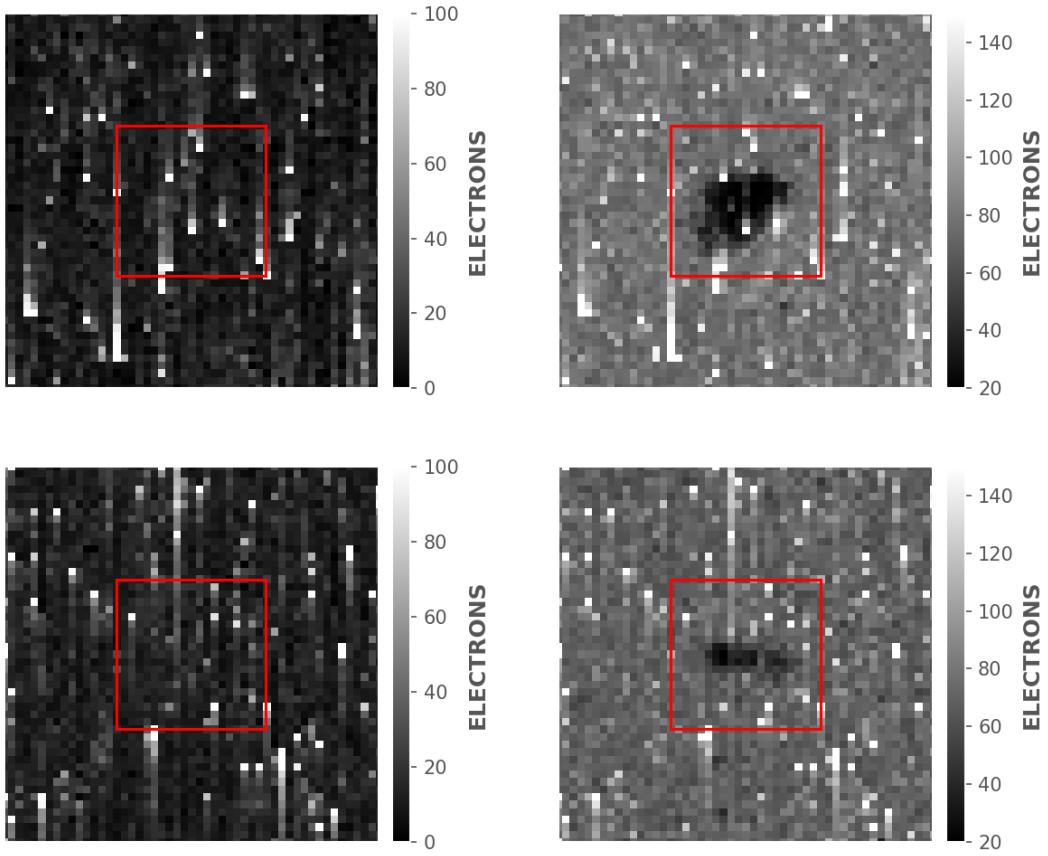

Figure 4 - Comparing the behaviors of the fleck-affected pixels. The top row shows the larger fleck and the bottom row shows the elongated fleck. A 20×20 pixel red square is shown for scale. The left column contains un-flashed data and the right column contains post-flashed data, both taken after the May 5th anneal. The un-flashed images show no sign of the flecks and no anomalous behavior in the underlying pixels.

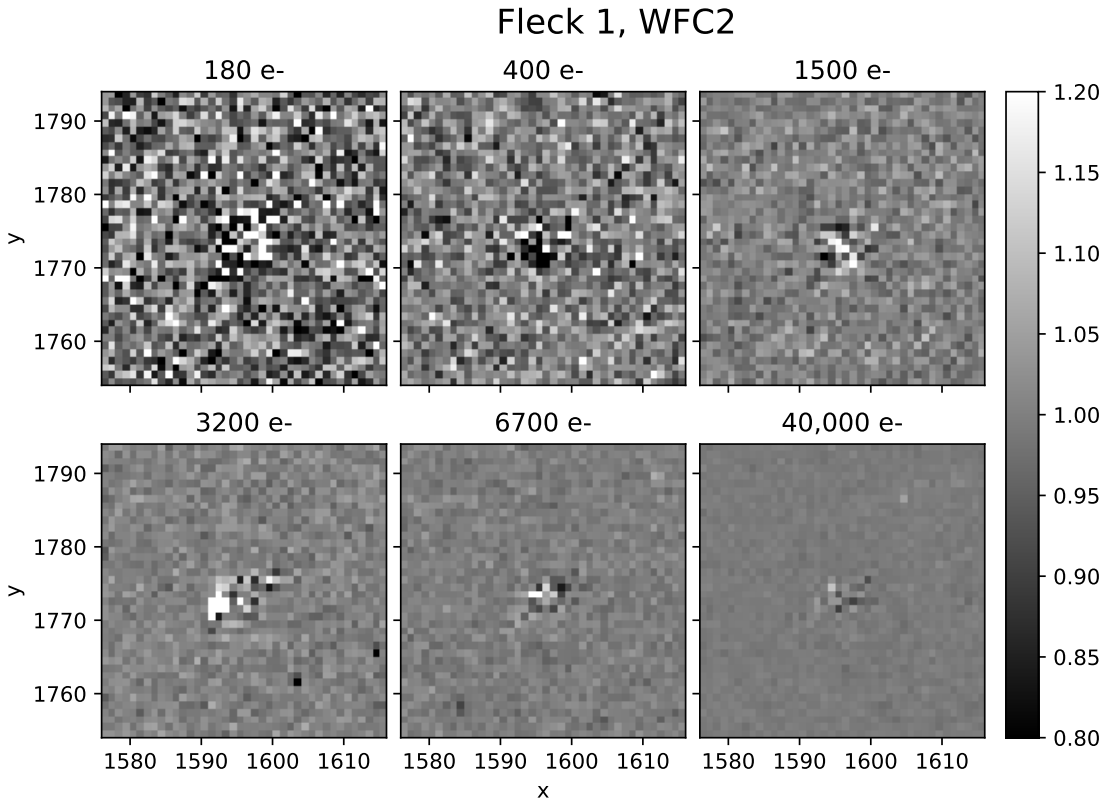

Figure 5 - Ratio of EPER flats observed in November 2017 and May 2017. Each panel shows the 40 × 40 pixel region containing the larger fleck (1) for the average signal level in the label.

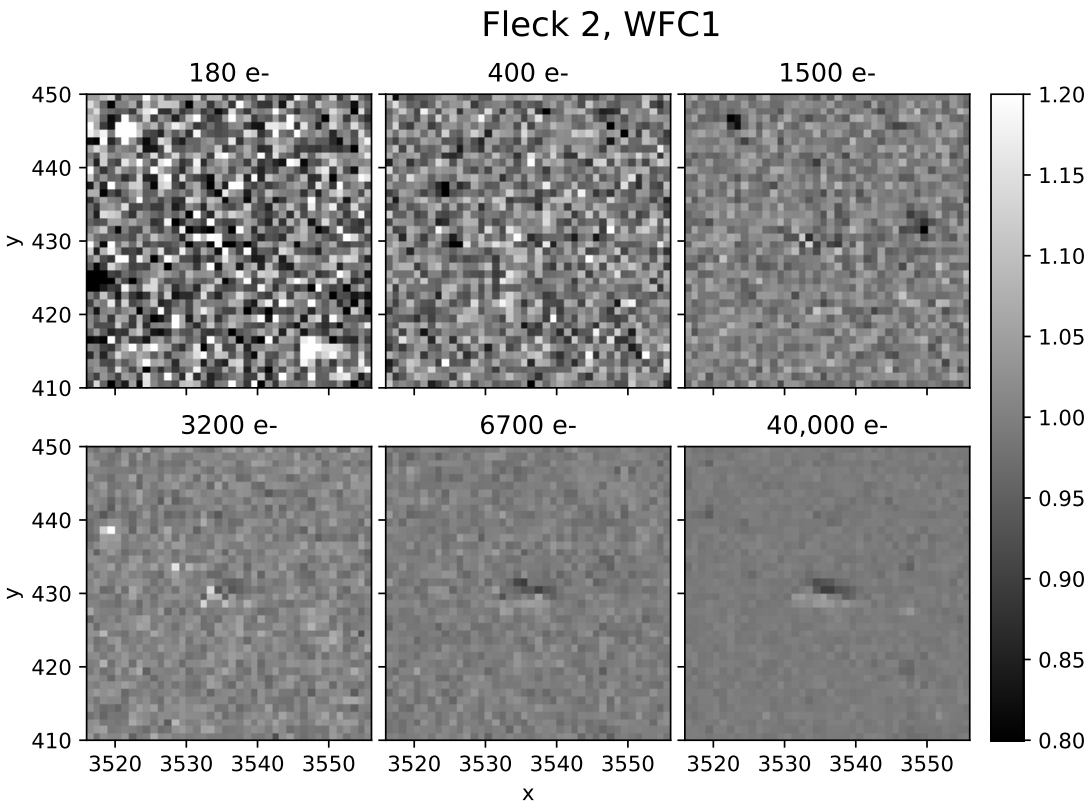

Figure 6 - Same as Figure 5 but for the elongated fleck (2) on WFC1.

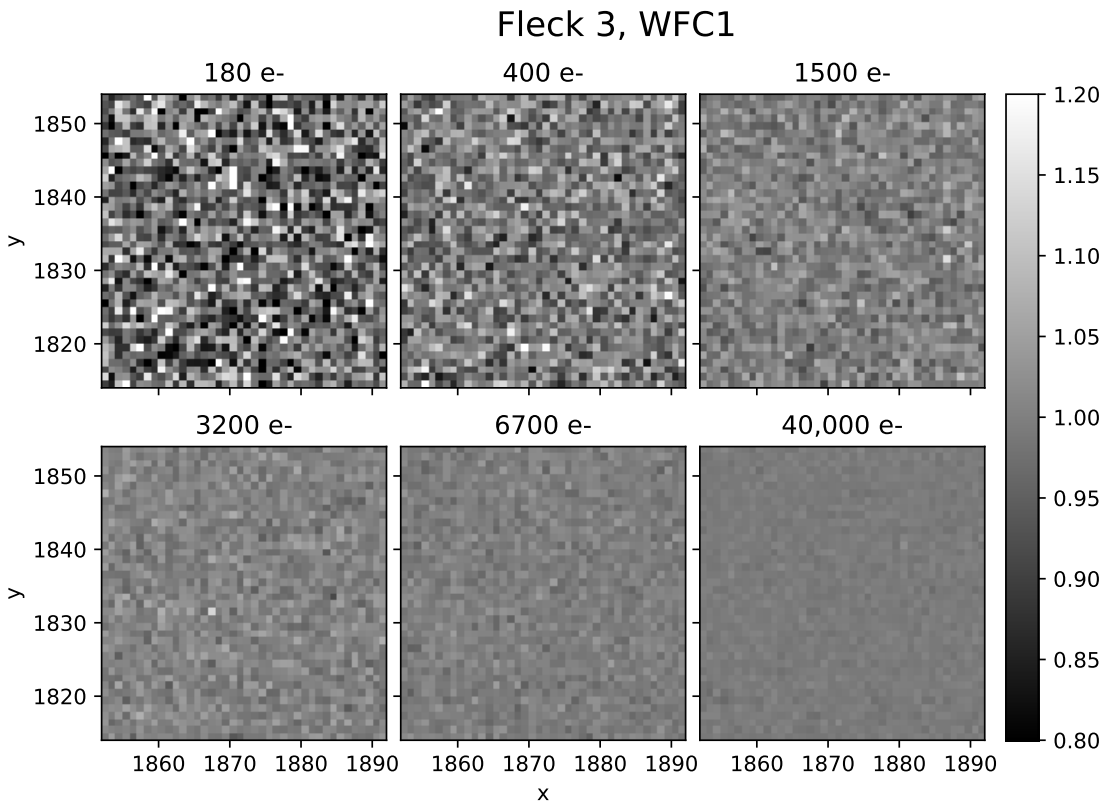

Figure 7 - Same as Figure 5 but for the tiny fleck (3) on WFC1.

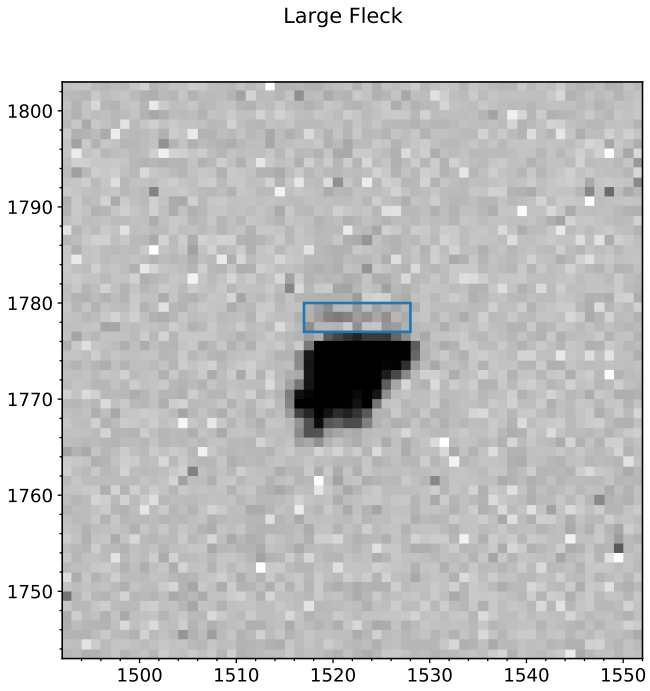

Figure 8 - A 60×60 pixel region containing the larger fleck in the average flashed short dark from August 2017. The blue rectangle outlines the shadow region that has a significantly lower signal than the background.

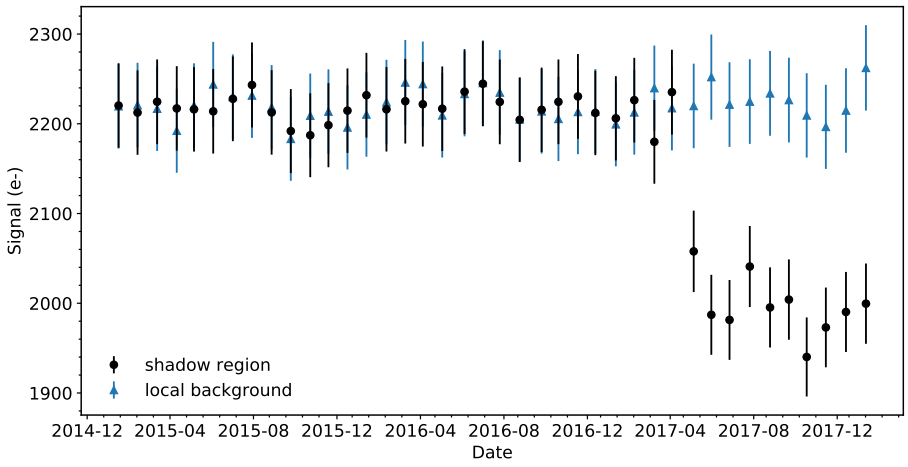

Figure 9 - Total signal as a function of time in the shadow region (black points) and a local empty background region (blue triangles).

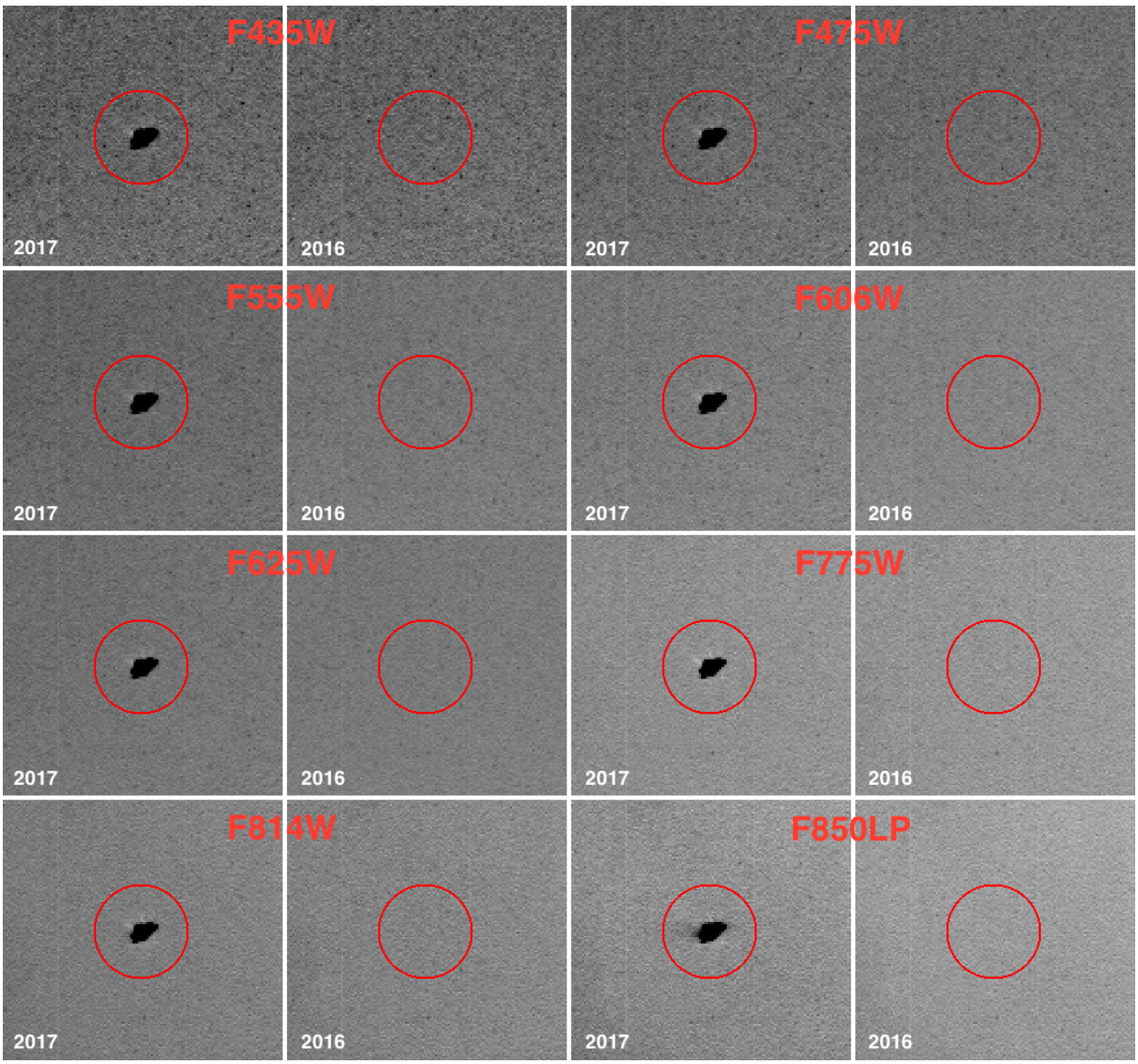

Figure 10 - Thumbnails in 8 broadband filters of the larger fleck on the WFC2 chip at (1521, 1773) in December 2017 and December 2016. The 2016 data show no artifact at this location. The red circle, provided for scale, is 25 pixels in radius.

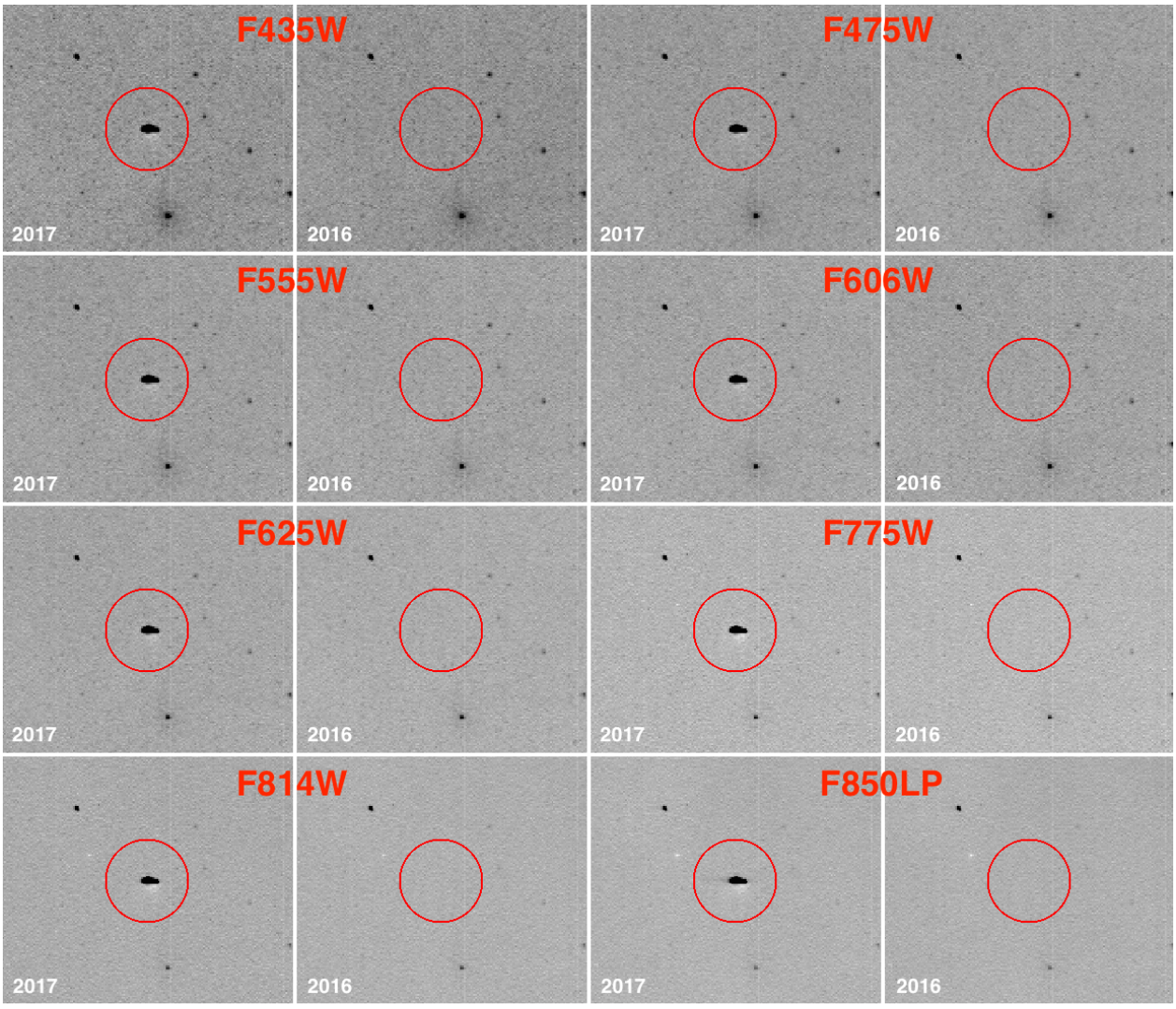

Figure 11 - Same as Figure 10, but for the elongated fleck at (3510, 355) on WFC1.

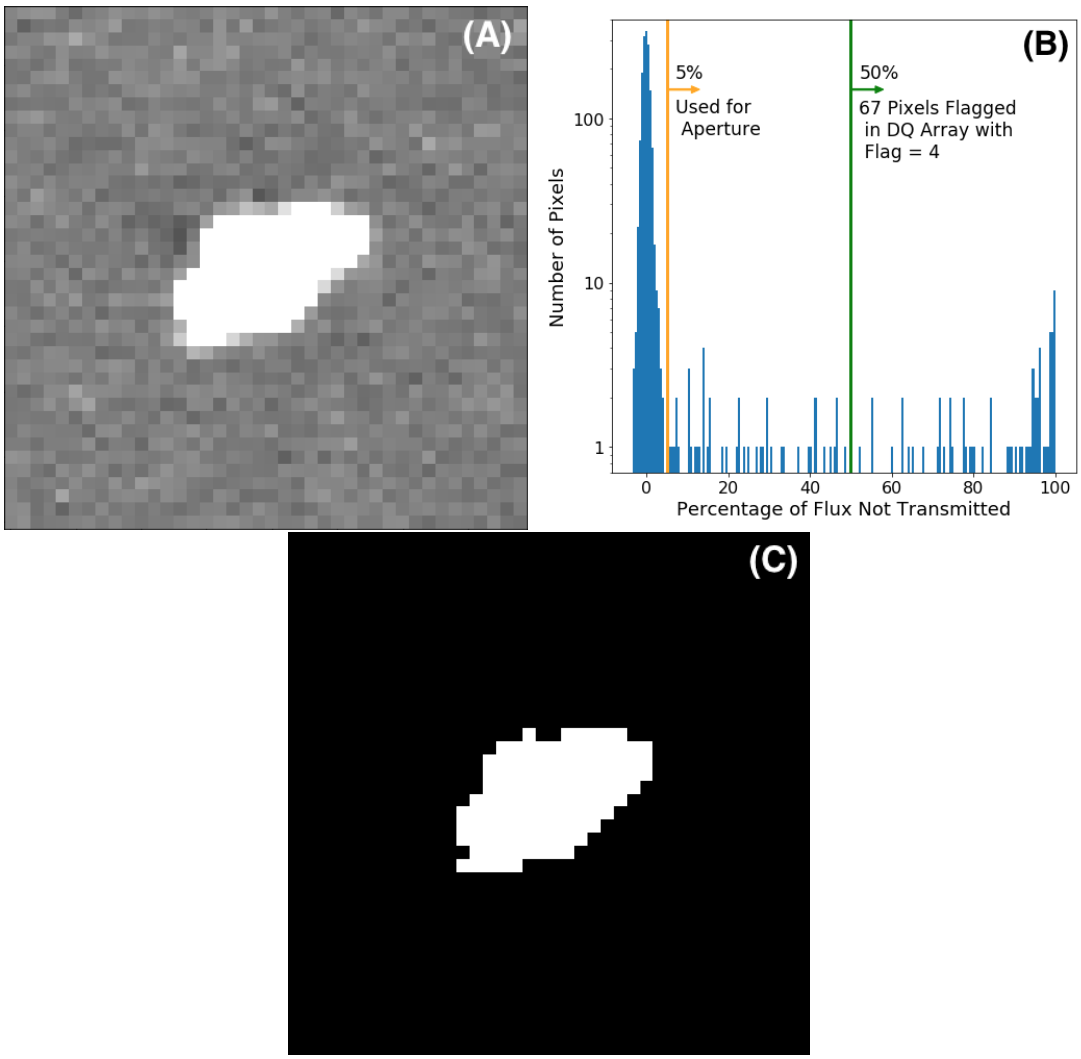

Figure 12 - Details of the F435W photometric analysis of the larger fleck on WFC2. Panel A (top left) shows a 40 × 40 pixel normalized image of the fleck with inverse colors such that white indicates lower flux measurements. Panel B (top right) plots a histogram of the percentage of flux not transmitted by each pixel based on the normalized, inverted image in Panel A. The vertical orange line on the left indicates a threshold of 5% lower flux used to separate the main distribution of local background pixels with a median of zero from outlier pixels associated with the fleck. The vertical green line indicates the 50% limit of the 67 outlier pixels which we flag as bad pixels in the DQ array. Panel C (bottom) displays the selected 5% outlier pixels in white. They form the photometric aperture for the larger fleck in the F435W data only.

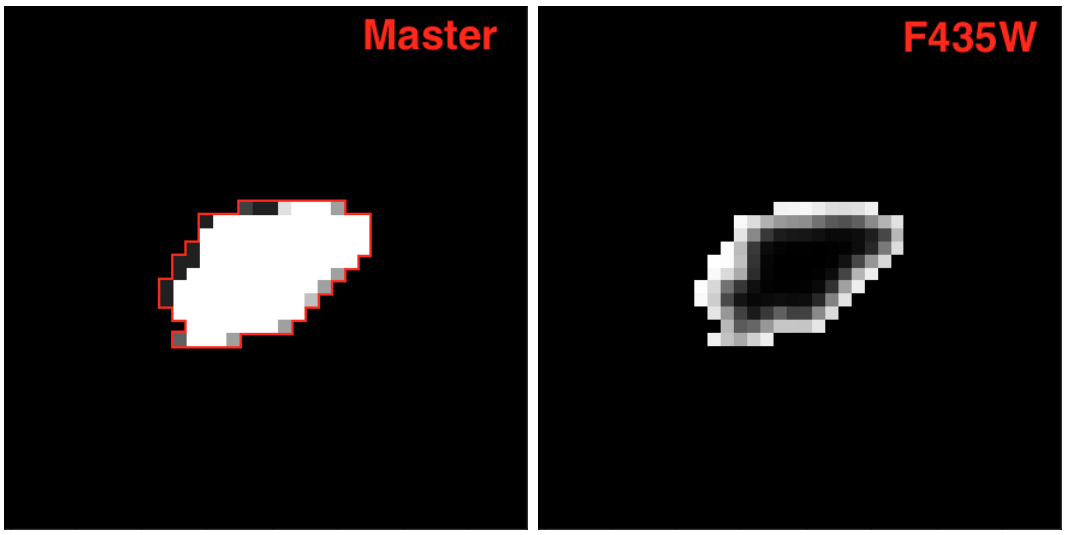

Figure 13 - (Left) The master photometric aperture. We summed the individual filter apertures (see Panel C in Figure 12) to show the frequency with which each pixel was considered to be within the fleck, where black was not selected in any filter, white was selected in all 8 filters, and the grey values map the range in between. The red outline represents the final shape of the master aperture. (Right) we show the master aperture applied to the F435W data to demonstrate the fit of the aperture to the larger fleck.

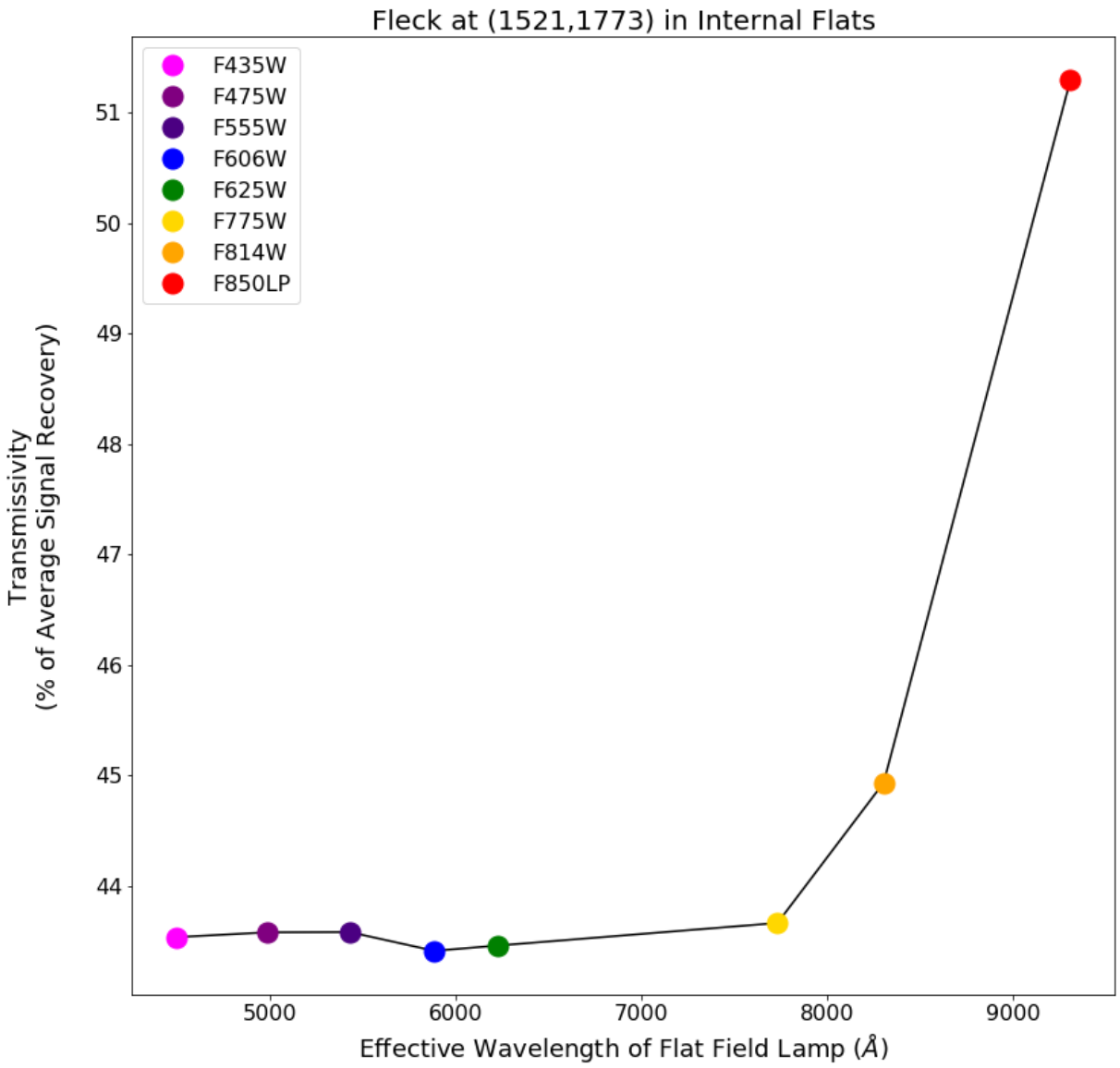

Figure 14 - We display the transmissivity, or the average percentage of the recovered signal, as a function of the effective wavelength of the flat field Tungsten lamp convolved with each filter. This is effectively a spectral energy distribution (SED) of the larger fleck. We include the errors in the plot, but they are smaller than the size of the symbol.

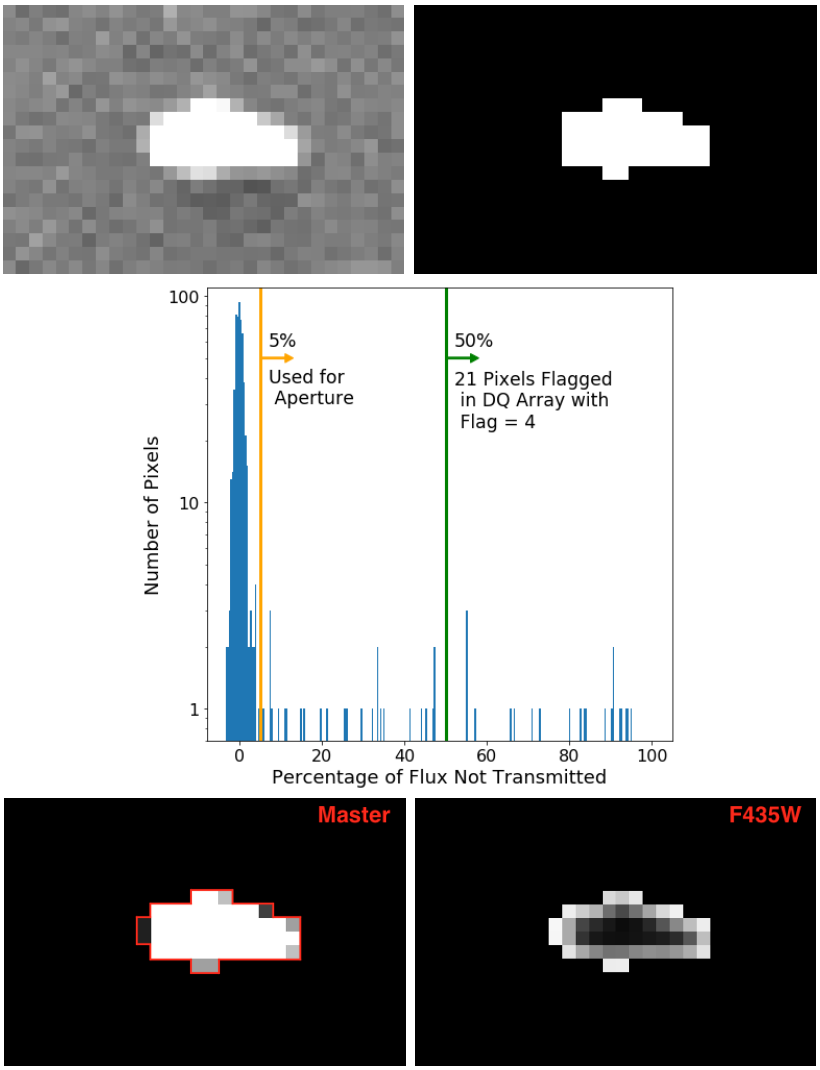

Figure 15 - Same as Figures 12 and 13 combined, but for the elongated fleck. We used a different image size (20×30 pixels) to fit the shape of the elongated fleck.

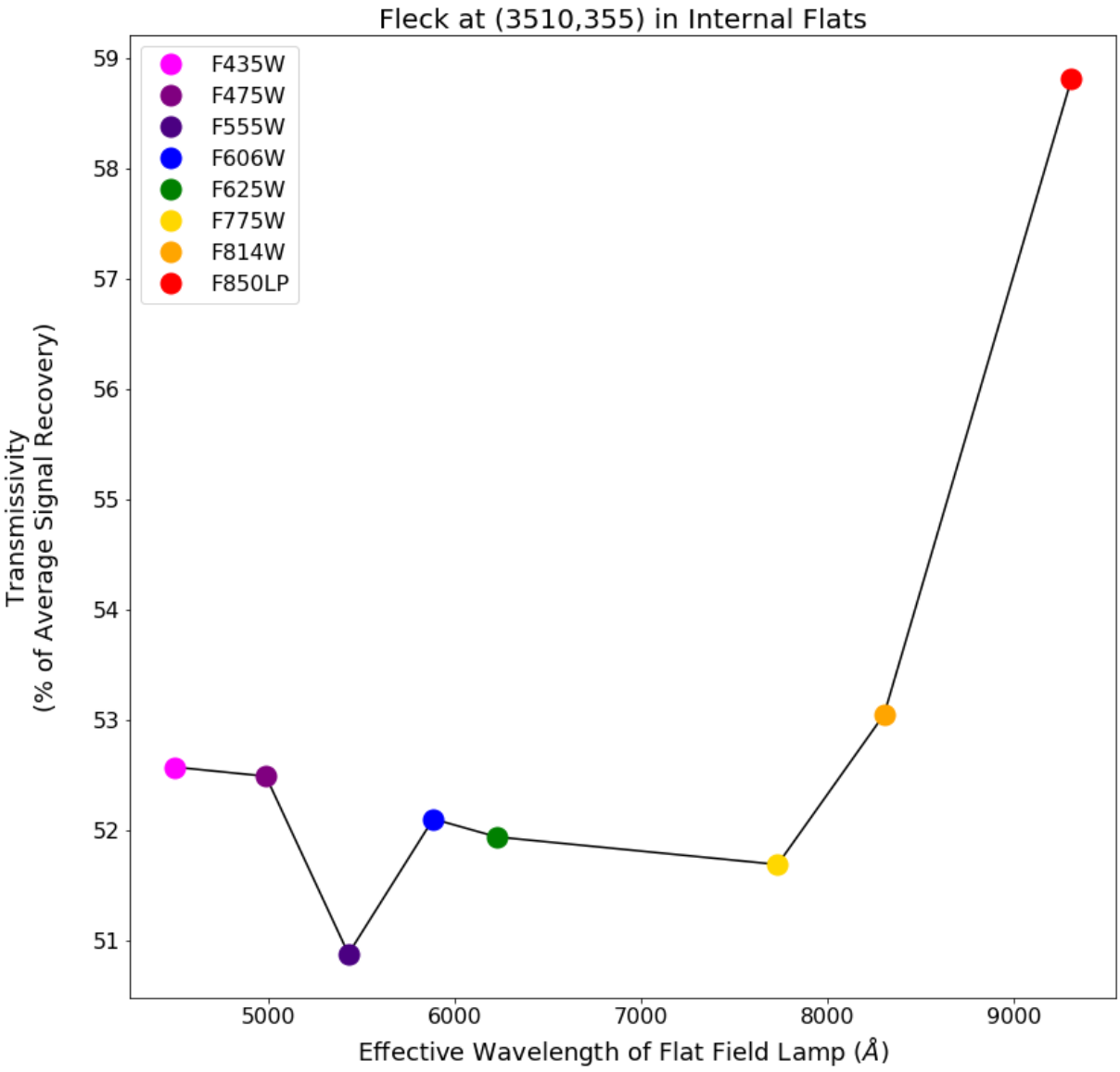

Figure 16 - Same as Figure 14, but for the elongated fleck. We believe the lower F555W measurement to be anomalous (see § 6.1 for more details).

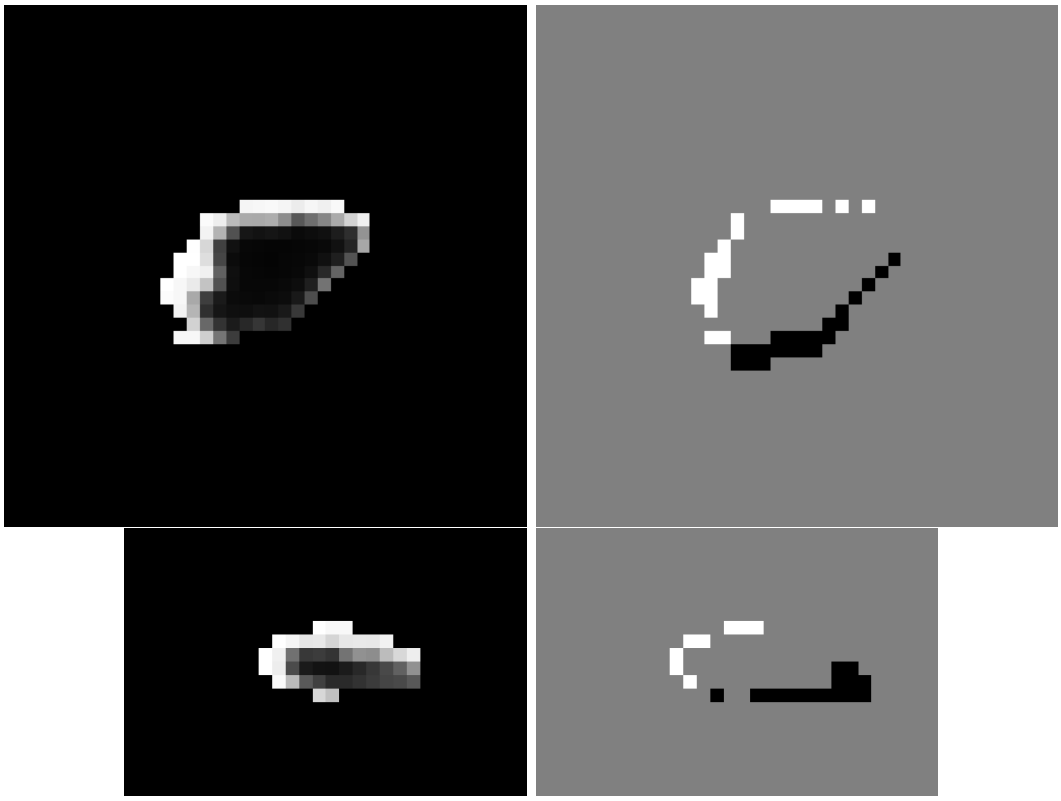

Figure 17 - (Top left) The master flat aperture generated for the larger fleck applied to the same 40×40 pixel location in the flashed superdark. Unlike the F435W image in Figure 13, the aperture does not fit the shape and position of the fleck in the superdark. (Top right) The difference between the flat aperture mask and one generated for the flashed superdark. (Bottom row) Same as the top row but for the corresponding 20×30 pixel images for the elongated fleck. The discrepancy has the same direction and magnitude for both flecks.

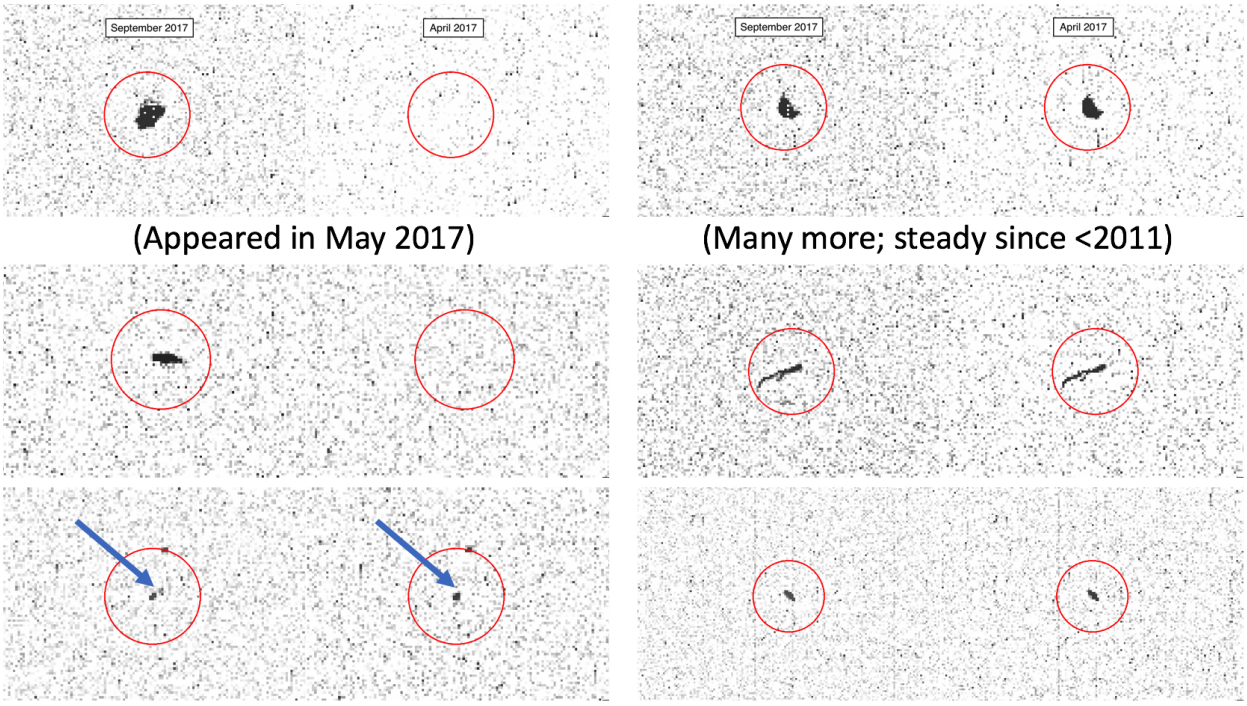

Figure 18 - (Left column) The three new flecks in short darks September and April 2017. (Right column) Three examples of existing image artifacts that have been stable over the lifetime of the ACS/WFC. Unlike the flecks, they exhibit no change during the May 2017 anneal.